HHS Public Access

Author manuscript

J Phys Chem B. Author manuscript; available in PMC 2019 December 18.

Published in final edited form as:

J Phys Chem B. 2019 April 25; 123(16): 3462–3474. doi:10.1021/acs.jpcb.9b02575.

Sequence Effects on Size, Shape, and Structural Heterogeneity in Intrinsically Disordered Proteins

Upayan Baul[†,§], **Debayan Chakraborty**[†], **Mauro L. Mugnai**[†], **John E. Straub**[‡], **D. Thirumalai**[*,†]

[†] Department of Chemistry, The University of Texas at Austin, Austin, Texas 78712, United States

[‡] Department of Chemistry, Boston University, Boston, Massachusetts 02215, United States

Abstract

Intrinsically disordered proteins (iDPs) lack well-defined three-dimensional structures, thus challenging the archetypal notion of structure—function relationships. Determining the ensemble of conformations that IDPs explore under physiological conditions is the first step toward understanding their diverse cellular functions. Here, we quantitatively characterize the structural features of IDPs as a function of sequence and length using coarse-grained simulations. For diverse IDP sequences, with the number of residues (N_T) ranging from 20 to 441, our simulations not only reproduce the radii of gyration (R_g) obtained from experiments, but also predict the full scattering intensity profiles in excellent agreement with small-angle X-ray scattering experiments. The R_g values are well-described by the standard Flory scaling law, $R_g = R_g^0 N_T^{\nu}$, with $\nu \approx 0.588$, making it tempting to assert that IDPs behave as polymers in a good solvent. However, clustering analysis reveals that the menagerie of structures explored by IDPs is diverse, with the extent of heterogeneity being highly sequence-dependent, even though ensemble-averaged properties, such as the dependence of R_g on chain length, may suggest synthetic polymer-like behavior in a good solvent. For example, we show that for the highly charged Prothymosin-α, a substantial fraction of conformations is highly compact. Even if the sequence compositions are similar, as is the case for α-Synuclein and a truncated construct from the Tau protein, there are substantial differences in the conformational heterogeneity. Taken together, these observations imply that metrics based on net charge or related quantities alone cannot be used to anticipate the phases of IDPs, either in isolation or in complex with partner IDPs or RNA. Our work sets the stage for probing the interactions of IDPs with each other, with folded protein domains, or with partner RNAs, which are critical for describing the structures of stress granules and biomolecular condensates with important cellular functions.

[*]**Corresponding Author** dave.thirumalai@gmail.com.

[§]**Present Address** Institute of Physics, Albert-Ludwigs-University of Freiburg, Hermann-Herder-Strasse 3, 79104 Freiburg, Germany.

ASSOCIATED CONTENT

Supporting Information

The Supporting Information is available free of charge on the ACS Publications website at DOI: 10.1021/acs.jpcb.9b02575. Details of the learning procedure used to calibrate the SOP-IDP model; comparison of experimental and simulated SAXS profiles (in the Kratky representation); comparison of simulated R_g values and those estimated from SAXS experiments; comparison with results from all-atom force fields; distributions of the shape parameters for all the IDP sequences; end-end (R_{ee}) and radius of gyration (R_g) distributions for all the IDP sequences; sequence compositional properties of the IDP sequences; contact maps for selected IDP sequences; and FASTA representation of the IDP sequences (PDF)

The authors declare no competing financial interest.

graphical abstract

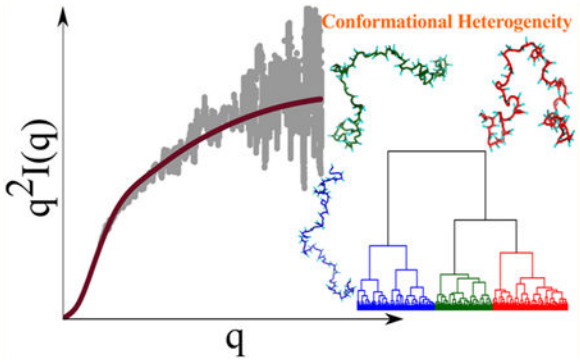

INTRODUCTION

The discovery that a large fraction of eukaryotic protein sequences are not ordered in isolation[1–7] has produced a paradigm shift in the commonly held view of structure—function relationship. Such sequences, referred to as intrinsically disordered proteins (IDPs), play key functional roles in diverse cellular processes, such as signal transduction[2,8] and vesicular transport,[9] and are also implicated in neurodegenerative disorders and other diseases.[3,10] Experimental realizations of folding coupled to binding partners and the more recent discovery of intracellular liquid—liquid phase separation[11] have further resulted in a concerted effort in describing the intramolecular and intermolecular interactions involving IDPs.[12–17] Recent estimates indicate that between 30 and 40% of eukaryotic proteomes are either intrinsically disordered or contain intrinsically disordered regions in otherwise folded proteins.[17,18] Despite the importance of IDPs, characterization of the sequence-dependent conformational properties of IDPs in isolation as well as their phase behavior remains largely qualitative.[14,16,19] Biologically relevant forms of IDPs do not fold into unique tertiary structures but explore a large number of distinct conformational states. In this sense, they are like synthetic polymers, whose conformations can only be characterized in statistical terms, such as the distribution of the radius of gyration, R_g, from which its dependence on the number of residues, N_T, can be calculated.[17,20] Two decades of experiments indicate that isolated IDPs typically behave as polymers in a good solvent based on the scaling of R_g with N_T.[21–23] However, the conformational ensembles of IDPs, which are instrumental in modulating their in vivo functionalities, strongly depend on the precise sequence, in addition to other external conditions, such as pH, temperature, and salt concentration.[24,25] Therefore, scaling laws alone cannot provide a faithful description of the physicochemical properties of IDPs. The complex sequence dependence poses a great challenge to purely theoretical approaches[26,27] and raises the need for computational models that can quantitatively account for the experimental data.

Small-angle X-ray scattering (SAXS) and single-molecule Förster resonance energy transfer (smFRET) have found the greatest applicability in the study of IDP conformational properties. [21,28] In addition, nuclear magnetic resonance (NMR) and fluorescence correlation spectroscopy (FCS)[24,28–31] have been used to characterize the structural ensembles and conformational dynamics of IDPs. SAXS experiments, which measure

structure factors, could be used to calculate the global conformational properties of IDPs, such as R_g and shape, whereas smFRET experiments are used to probe distances between specific labeled residues along the polypeptide chain. With SAXS, the measured structure factor, $I(q)$, as a function of the wave vector q, at small values of q is often used to estimate R_g using the Guinier approximation.[32] However, the sequence-specific conformational ensembles are not directly available from SAXS experiments, and usually, techniques based on ensemble optimization are invoked to map scattering profiles to representative structures.[33]

A complementary approach involves computer simulations that employ force fields to generate IDP ensembles, which embody the key experimental observables. It is tempting to exploit an all-atom representation for IDPs and the surrounding environment in order to characterize their conformations. Indeed, great progress is being made in devising new force fields, which make systematic updates to the existing water models or protein interaction potentials.[34–38] Systematic benchmarking has revealed that although all-atom force fields provide the much needed microscopic insight into the conformational dynamics of IDPs, the associated ensembles often tend to depend on the details of the parameterization.[39,40] A simpler description of the protein molecule based on systematic coarse graining often provides a complementary route toward probing the conformational dynamics of IDPs.[15,41,42] We and others have previously exploited coarse-graining strategies with great success in applications of protein folding and kinetics[43–45]. In this work, we introduce a self-organized polymer (SOP) coarse-grained model for IDPs (SOP-IDP), which not only recapitulates the wealth of experimental SAXS data, but also delineates the complex interplay between sequence, structure, and aspects of conformational heterogeneity that have been largely unexplored in much of the previous studies.

We show that for IDPs of varying lengths and sequence composition, the R_g values are in accord with Flory's scaling law. The calculated R_g values from simulations are generally in good agreement with those extracted from SAXS data. The simulations accurately reproduce the measured SAXS profiles, thus allowing us to provide insights into the shape and conformational fluctuations, which govern their functions. The ensembles of conformations of all the IDPs are heterogeneous, with sequence being a key determinant of the relative populations of different substates. Our findings using SOP-IDP simulations suggest that the phases of IDPs cannot be predicted solely based on sequence compositional properties but require complete statistical characterization of the IDP ensembles.

METHODS

Development of the Model.

In the SOP-IDP model, except for glycine and alanine, the amino acid residues are represented using a backbone and a side-chain (SC) bead. We use the C_α atoms to model glycine and alanine owing to their small SCs. The radii of the individual beads are given in Table S1 of the Supporting Information. The energy function in the SOP-IDP model is

$$E = -\sum_{i=1}^{N_B} \frac{k}{2} R_0{}^2 \log\left(1 - \frac{\left(r_i - r_{ref,i}\right)^2}{R_0^2}\right) + \sum_{i=1}^{N_{\text{loc}}} \epsilon_{\text{loc}} \left(\frac{\sigma_i}{r_i}\right)^6 + \sum_{i,j}{}' \frac{e_i e_j \exp\left(-\kappa r_{ij}\right)}{\varepsilon r_{ij}} + \sum_{i=1}^{N_{\text{BB}}} \epsilon_{\text{BB}} \left[\left(\frac{\sigma_i}{r_i}\right)^{12} - 2\left(\frac{\sigma_i}{r_i}\right)^6\right] + \sum_{i=1}^{N_{\text{BS}}} \epsilon_{\text{BS}} \left[\left(\frac{\sigma_i}{r_i}\right)^{12} - 2\left(\frac{\sigma_i}{r_i}\right)^6\right] + \sum_{i=1}^{N_{\text{SS}}} \epsilon_{\text{SS}} |\epsilon_i - 0.7| \left[\left(\frac{\sigma_i}{r_i}\right)^{12} - 2\left(\frac{\sigma_i}{r_i}\right)^6\right] \quad (1)$$

The first term in eq 1, for a chain with N_B bonds, represents bonded interactions, which are described using a finitely extensible nonlinear elastic (FENE) potential. The purely repulsive second term acts only between bead pairs (total number N_{loc}) that are not covalently bonded but belong to residues separated by ≤2 along the polypeptide chain. It represents the excluded volume interactions that prevent unphysical bond crossing between pairs of beads that closely follow one another along the polymer chain. The third term is a screened Coulomb potential that accounts for electrostatic interactions between all pairs of charged residues. The charge corresponding to a residue is assigned to the SC. The titratable residue histidine is treated as neutral in the model, unless it is experimentally determined to be in the protonated state. The parameters κ and ε in the third term in eq 1 are the inverse Debye length and the dielectric constant, respectively. These three terms were previously used in protein folding and related studies,[43,44,46] where the justifications for their choices are given.

The final three terms in eq 1 represent interactions between backbone—backbone (BB), backbone—side-chain (BS), and side-chain—side-chain (SS) beads. The total numbers of such BB, BS, and SS pairs are, respectively, N_{BB}, N_{BS}, and N_{SS}. Interactions between the SCs depend only on the identities of the amino acids without bias toward any specific structure. The parameter ϵ_i in the final term in eq 1 is obtained from the Betancourt—Thirumalai statistical potential.[47] The ϵ_i values are unique to each pair of amino acid residues, and hence, depend explicitly on the IDP sequence. In eq 1, the three parameters ϵ_{BB}, ϵ_{BS}, and ϵ_{SS} set the energy scales corresponding to the nonlocal interactions and are the only free parameters in the energy function. We determine the initial values of ϵ_{BB}, ϵ_{BS}, and ϵ_{SS} in a top-down fashion by using the SAXS data (R_g and $I(q)$) for only three short IDPs ($24 \le N_T \le 131$) as constraints in the parameterization scheme. Subsequently, to find the optimum values of the parameters, only the experimental R_g estimates for three long IDP sequences ($202 \le N_T \le 441$) were used as constraints in the parameterization scheme. Further details of this learning procedure are provided in the Supporting Information.

Comments on the Parameter Values.

The values of the parameters, which were obtained using a learning procedure described in the Supporting Information, in the SOP-IDP model are

$$\epsilon_{BB} = 0.12\text{kcal/mol}, \quad \epsilon_{BS} = 0.24\text{kcal/mol}, \quad \epsilon_{SS} = 0.18\text{kcal/mol} \tag{2}$$

which in units of $k_B T$ (T = 298 K) are $\epsilon_{BB} = 0.2, \epsilon_{BS} = 0.4, \epsilon_{SS} = 0.3$ These values differ from the ones used to describe globular proteins,[48] which were obtained in order to describe their folding thermodynamics at zero denaturant concentration ([C]). As [C] increases, the stability of the folded states decreases, which we accounted for phenomenologically using transfer free energies, thus creating the SOP-molecular transfer model (MTM).[48] The effective interaction parameters ϵ_{BB}, ϵ_{BS}, and ϵ_{SS} are expected to decrease as [C] increases, so that at high [C], the statistical properties of the denatured state ensemble (DSE) of globular proteins and IDPs, such as R_g, would exhibit the scaling $R_g \approx 0.20 N_T^{\nu}$, with $\nu \approx 0.588$.[49] Because the R_g scaling of DsEs of globular proteins at high denaturant concentrations is statistically equivalent to those for IDPs (hence the plausible relevance of IDPs to the SAXS-FRET controversy), it is not surprising that the optimal values for the SOP-IDP model (eq 2) differ from the [C] = 0 values.[48] The values of ϵ_{BB}, ϵ_{BS}, and ϵ_{SS} for globular proteins in water, respectively, are 4.6, 1.7, and 1.7 times larger than the values for IDPs (eq 2).

If the above reasoning is correct, then we ought to obtain reasonably accurate R_g values for globular proteins at high denaturant concentrations using the parameters given in eq 2. After all, at high [C], the unfolded states of globular proteins are statistically equivalent to IDPs. To this end, we simulated the sequence corresponding to the highly charged ubiquitin (PDB ID: 1UBQ) molecule using the current SOP-IDP force field. The estimated R_g for ubiquitin using the SOP-IDP model is 2.51 and 2.55 nm at 150 and 1000 mM monovalent salt concentrations, respectively. These values compare well with the R_g for the DSE of ubiquitin (≈2.56 nm, see, e.g., Figure 4A in Gates et al.[49] and Figure 2A in Reddy et al.[50] at high denaturant concentration). The simulations described in Reddy et al.[50] were carried out using the parameters described in Liu et al.[48] and taking into account the effect of denaturants using MTM. These new simulations for ubiquitin using the SOP-IDP model are gratifying because the SOP-MTM[50] and the current model were developed using entirely different methods for different purposes. This shows that the parameters for the IDP model describe well the properties of globular proteins at high denaturant concentrations (8 M GdmCl), in line with the expected statistical equivalence of their ensembles with IDPs. However, as pointed out in the Discussion section, the parameters will not be accurate in the sense found for IDPs for real globular proteins.

Simulations.

We used the LAMMPS molecular dynamics simulator for all the simulations,[51] which were performed using underdamped Langevin dynamics.[52] The equations of motion were integrated with a time step of 30 fs. To obtain statistically meaningful results, we carried out 10 independent simulations for each system, which we ascertained are sufficient to obtain converged results. Each trajectory was equilibrated for 10^8 simulation steps, following which the production runs were carried out for 2×10^8 simulation steps for sequence lengths

<130 and 5×10^8 simulation steps for longer sequences. Visual molecular dynamics (VMD) was used for visualization, as well as some data analyses.[53]

In our simulations, all the nonbonded interaction terms in eq 1 were implemented in their truncated and shifted forms, with the cutoff separation for short-range interactions set at 2.4 nm. The cutoff separation for the screened Coulomb potential was consistently chosen to be greater than $4\kappa^{-1}$. The inverse Debye length (κ) was determined from the corresponding monovalent salt concentrations employed in the simulations. We set the dielectric constant, $\varepsilon = 78$.

Data Analyses.

The simulated SAXS profiles were computed using the Debye formula

$$I(q) = \sum_{i=1}^{N_{tot}} \sum_{j=1}^{N_{tot}} f_i(q) f_j(q) \frac{\sin(qr_{ij})}{qr_{ij}} \tag{3}$$

with q-dependent structure factors ($f(q)$), which were reported elsewhere.[54] In eq 3, N_{tot} is the total number of beads in a given IDP.

Hydrodynamic Radius, R_h.

Dynamic light scattering and FCS experiments[9,55–57] are routinely used to measure R_h. The value of R_h for a polymer is calculated as the radius of a hard sphere that has the same effective diffusive behavior as the polymer. We computed R_h from the simulations using

$$\frac{1}{R_h} = \frac{1}{N_{tot}^2} \left\langle \sum_{i \neq j} \frac{1}{r_{ij}} \right\rangle \tag{4}$$

where N_{tot} is the total number of beads in the IDP model and r_{ij} is the distance between beads j and i. The angular brackets denote the ensemble average.

Shape Parameters.

We use Δ and S to characterize the shapes offolded and unfolded proteins,[58,59] which are defined as

$$\Delta = \frac{3}{2} \frac{\sum_{i=1}^{3} (\lambda_i - \bar{\lambda})^2}{(3\bar{\lambda})^2}, \quad s = \frac{\prod_{i=1}^{3} (\lambda_i - \bar{\lambda})}{\bar{\lambda}^3} \tag{5}$$

where λ_i are the eigenvalues of the gyration tensor and $\bar{\lambda} = (\lambda_1 + \lambda_2 + \lambda_3)/3$.[58] By definition, $R_g^2 = 3\bar{\lambda}$. The Δ parameter characterizes the asphericity of conformations and is bound between 0 (perfectly spherical) and 1 (linear). The shape parameter S, which is negative (positive) for oblate (prolate) ellipsoids, satisfies the bound $-1/4 \leq S \leq 2$.[60]

Hierarchical Clustering.

To identify representative conformations populating the IDP ensembles as well as characterize their structural heterogeneity, we performed hierarchical clustering[61] using a pairwise distance metric D_{ij}, defined as

$$D_{ij} = \left(\frac{1}{N_{\text{pairs}}} \sum_{a,b} \left| \left(r_{a,b}^{\,i} - r_{a,b}^{\,j} \right) \right|^2 \right)^{1/2} \tag{6}$$

where $r_{a,b}{}^{i}$ and $r_{a,b}{}^{j}$ are the pairwise distances between the C_α atoms a and b in snapshots i and j, respectively, and N_{pairs} is the total number of C_α pairs. The terminal C_α atoms were excluded in the evaluation of the distance matrix. The Ward variance minimization criterion,[62] as available within the *scipy* module, was employed to identify the distinct clusters. The hierarchical organization of clusters was visualized in the form of dendrograms. The structure exhibiting the lowest root-mean-square-deviation with respect to all the other members is identified as the representative structure of a given cluster.

RESULTS

SOP-IDP Model Accurately Reproduces Experimental SAXS Profiles.

We used the SOP-IDP model (see Methods and Supporting Information for details) to calculate a variety of measurable structural properties for different IDP sequences. Twelve of these, including the initial training set consisting of Histatin-5, ACTR, and hNHE1, are sequences with lengths ranging from 24 to 273 that are unrelated in composition and biological functions.[6374] The computed scattering profiles, $I(q)$, as a function of the scattering vector q, bear close resemblance to those obtained from SAXS experiments, particularly in the low q regime, which describes the global structure of IDPs (Figure 1). The scattering profiles depicted in the Kratky representation $(q^2 I(q)/I(0)$ vs q, Figures S1 and S2) are also accurate at low q values. The level of agreement between our simulations and experiment is further quantified by calculating the normalized squared deviation, δ^2 (Table S2). The δ^2 values conclusively show that for most sequences, the overlap between the calculated and experimental SAXS profiles remains good up to $qR_g \approx 3$, well beyond the range of validity of the Guinier approximation, normally taken to be $qR_g \approx 1.3$. Hence, the SOP-IDP model not only accurately describes the global shapes of IDPs, but also likely captures the structural details on smaller length scales. In some cases, the agreement with experimental profiles deteriorates at $qR_g > 3$, perhaps owing to a combined effect of the increased experimental noise and the coarse-grained nature of the model.

Wild-Type Tau Proteins and Their Variants.

In notable SAXS experiments, Svergun and co-workers measured the structure factors of the wild-type (WT) 441 residue human Tau protein, as well as artificial sequence constructs generated through truncation and merger of segments.[75] We simulated 11 such artificial constructs (Supporting Information contains the sequences), in addition to the full length WT sequence using the SOP-IDP model, thus covering the full range of sequence lengths ($99 \leq N_T \leq 441$) considered in the experiments. The scattering profiles for the Tau sequences are shown in Figure 2.

As is evident from the δ^2 values (Table S2), the simulated and experimental profiles are in good agreement. It should be emphasized that we used only 5 (Histatin-5, ACTR, hNHE1, K32, and hTau40) of the 20 IDPs shown in Figures 1 and 2 to learn the parameters in the model (described in the Supporting Information). Of these, we used only the R_g values for K32 and hTau40 as a constraint to determine a single parameter and not the SAXS profiles. Therefore, the good agreement between the simulated and experimental SAXS profiles, across the sample set, which is diverse in terms of sequence composition, length, and charge densities, is truly an emergent property of our model. In addition, we also show in the Supporting Information that the calculated $I(q)$ as a function of q for the 24-residue RS peptide is in excellent agreement with experiments as are the results based on one of the recently introduced atomically detailed force fields.[38] Because of its predictive power over a wide range of sequence space, we anticipate that the SOP-IDP model will be efficacious in applications that require a faithful description of conformational ensembles, among other properties. We have predicted $I(q)$ for two other IDPs in the Supporting Information, which await future validation.

Dependence of Radius of Gyration and Hydrodynamic Radius on Sequence Length.

Given the accurate reproduction of the SAXS profiles (Figures 1 and 2) for most IDPs, it is not surprising that the R_g values computed from simulations are also in accord with the experimental values (Figure S3). The scaling of R_g with sequence length (N_T), fitted using the calculated or experimental R_g values, follows $R_g \approx 0.20 N_T^{\nu}$ nm, with $\nu \approx 0.588$ (Figure 3a), which naively suggests that in the experimental conditions, the IDPs might be in a good solvent. However, this is not the case (see below).

We also calculated the hydrodynamic radii, R_h, from the conformational ensemble using eq 4. The computed values of R_h are shown in Figure 3b and are tabulated in Table S3 of the Supporting Information. Though not equal in magnitude, both R_g and R_h (measurable from NMR for example) should show the same scaling with N_T with identical values of ν (Figure 3a,b).[76] However, this scaling behavior does not imply that these IDPs behave as random coils (RC).[32] Indeed, the R_h/R_g ratios from simulations deviate substantially from the established theoretical limits, which are 0.665 and 0.640 for an ideal chain and a polymer in a good solvent, respectively (Figure 3c). As N_T increases beyond 300, R_h/R_g becomes insensitive to sequence length (Figure 3c), indicating that the observed deviations may not be due to finite size effects.

Distributions of Radius of Gyration (R_g) and End-End Distances (R_{ee}).

If the solution conditions used in experiments are good solvents for IDPs, as the R_g and R_h scaling with N_T imply (Figure 3), then it should be reflected in the distribution $P(R_{ee})$ of the end-end distance (R_{ee}), which is rigorously known for a polymer and an ideal chain in a good solvent. Therefore, comparing the simulated distributions to the rigorous functional forms provides a stringent test of the solvent quality. The $P(R_{ee})$ distributions, with R_{ee} measured as the separation between the backbone atoms at the termini, are shown in Figure 4a,b (see also Figures S12 and S13 in the Supporting Information). As a general rule, we find that the $P(R_{ee})$ for IDPs closely resemble the theoretical result for a RC. However, for

specific sequences, the distributions are more skewed toward the ideal or the Gaussian chain limit.[32,77] The deviations from the RC limit based on the theoretical predictions are likely due to nonlocal electrostatic interactions and sequence composition (see below). Figure 4a shows that the $P(R_{ee})$ distribution for Prothymosin-α differs substantially from both the theoretical limits. The deviation can be attributed to the high fraction of charged residues (~58%).

Sequence Matters.

Interesting sequence-specific effects on the $P(R_{ee})$s are also observed for the Tau protein constructs, in spite of their common parent sequence. The $P(R_{ee})$s for the majority of the Tau protein constructs show excellent agreement with the theoretical $P(R_{ee})$ for a RC (see Figure 4b for K19 and K16 and also Figure S11 in the Supporting Information) and deviate substantially from that for an ideal chain. Deviations from the RC behavior are found for 5 out of the 12 Tau sequence constructs, namely, K25 (Figure 4b), K23, K44, hTau23, and the WT sequence, hTau40 (Figure S13 in the Supporting Information). The $P(R_{ee})$s for these sequences show increased propensities for smaller R_{ee}, as can be seen from Figure 4b for the K25 Tau construct. These sequence-specific deviations from average RC-like behavior are also discernible in the distributions of R_g values, as shown in Figure 4c,d. In Figure 4e, the ratio of R_g to root-mean-square R_{ee} is shown as a function of N_T. This ratio is 0.406 for a RC and 0.408 for a Gaussian chain.[32] Interestingly, even for those IDPs, whose $P(R_{ee})$ coincides with the theoretical predictions for RCs, the $R_g/\langle R_{ee}^2\rangle^{1/2}$ values deviate from the theoretical limits. This deviation becomes particularly pronounced as N_T increases, most notably for the longer Tau protein constructs.

The Tau sequences, which do not conform to standard polymer behavior, namely, K25, K23, K44, hTau23, and hTau40, do not differ appreciably from the rest of the sequence constructs in terms of conventional sequence compositional parameters that are often used to rationalize their shapes (Table S4 in the Supporting Information). This apparent incongruity could be rationalized in terms of ensemble-averaged contact maps obtained from simulations (see the Discussion section). We document below that the deviation from the theoretical RC limit is in fact a direct manifestation of the sequence-dependent conformational heterogeneity.

Shape Parameters Are Sequence-Dependent.

The sequence-specific shape fluctuations of IDPs can be gleaned from the distributions of their shape parameters, Δ and S (see eq 5 in Methods). The calculated values of Δ and S indicate that the conformations of IDPs can be described as prolate ellipsoids (Table S3 in the Supporting Information). In Figure 5, we show the distributions for four IDP sequences, and the rest are included in the Supporting Information (Figures S6-S9).

Figure 5a shows that Prothymosin-α has a high preference for extended conformations, while the structural ensembles for the K25 construct and α-Synuclein are closer to being spherical. In contrast, the shape parameters for An16 are homogeneously distributed, suggesting that elongated and spherical conformations are equally probable. This systematic trend is also reflected in the distributions of S (Figure 5b), where the bias toward prolate

conformations is maximal for Prothymosin-α and minimal for K25. The large dispersions in $P(\Delta)$ and $P(S)$ make the calculation of the mean values, listed in Table S3 of the Supporting Information, not meaningful (see Supporting Information for elaboration). For comparison, the average values of Δ and S for Gaussian chains are 0.52 and 0.87, respectively, and the corresponding estimates for an equivalent polymer in a good solvent are 0.55 and 0.91, respectively.[78] Overall, the shape fluctuations of the IDPs allude to a sequence-dependent heterogeneity of conformational ensembles. This aspect, which seems characteristic of the conformations of the IDPs explored here, is discussed in more detail below.

IDP Conformations Are Structurally Heterogeneous.

The distributions of R_g and R_{ee}, as well as their deviations from RC-like behavior for certain IDPs, suggest that the equilibrium populations of different conformations populating the IDP ensemble depend on the sequence. To illustrate the importance of conformational fluctuations in determining the statistical properties of IDPs, we consider representative examples: Prothymosin-α, α -Synuclein, An16, and the K25 construct from the family of Tau proteins.

To obtain insights into the structural ensembles and reveal their heterogeneous nature, we performed hierarchical clustering of the IDP conformations. Hierarchical clustering not only provides a means to quantify the contrasting features of the structural ensembles, which are evident from the Δ and S distributions, but also aids in visualizing the extent of the underlying conformational heterogeneity. We note that several authors have used "heterogeneity" as a concept to underscore the differences between homopolymers and IDPs.[79–81] More recently, this idea has also been suggested to explain the apparent lack of agreement between the R_g values measured using SAXS and those inferred from FRET experiments.[82–84]

The results from the clustering analyses of α-Synuclein and the K25 Tau construct are shown in Figure 6. The conformational ensembles corresponding to An16 and Prothymosin-α are depicted in Figure 7. The appropriate number of clusters for each sequence was determined by evaluating the largest distance jumps in the corresponding dendrograms using the elbow method.[85] Figures 6 and 7 show that our clustering scheme is robust, and the various families are clearly demarcated on a two-dimensional projection of the conformational landscape onto the R_g and R_{ee} coordinates.

α-Synuclein and K25.—The equilibrium ensemble of α -Synuclein (Figure 6) partitions into at least three clusters and consists of a large population of relatively compact structures (43.9%). Both semiextended and fully extended structures are populated to a lesser extent, with occupation probabilities of 27.5% and 28.6%, respectively. As is evident from the dendrogram (Figure 6), the equilibrium ensemble of the K25 Tau protein construct is overwhelmingly dominated by relatively compact structures, with the overall contribution being 67.1% to the net population. This trend is also reflected in the two-dimensional conformational landscape, where the region with small R_g and R_{ee} values is associated with the highest density. The shape of the conformational landscapes for both α-Synuclein and

K25, as well as the relative cluster sizes, is commensurate with the observed deviations from a RC-like behavior.

An16 and Prothymosin-α.—The equilibrium ensemble of An16 (Figure 7) consists of approximately equal contributions from relatively compact, semiextended, and extended structures, with the populations being 32.5%, 31.7%, and 35.8%, respectively. The relative populations suggest that no specific conformation is particularly favored for An16, which is consistent with a RC-like behavior.

For the Prothymosin-α sequence, the ensemble of conformations partitions into at least three clusters (Figure 7). Although naively, we expect that, due to the high value of net charge, there would be an overwhelmingly large population of extended structures for Prothymosin-α, clustering of conformations shows otherwise. While conformations exhibiting high R_g and R_{ee} values contribute maximally to the equilibrium population (37.1%), relatively compact conformations constitute the second largest cluster and account for as much as ≈35.6% of the conformational ensemble. Configurations having intermediate values of R_g and R_{ee} or the semiextended structures have the lowest occupation probability (27.3%).

Overall, the systematic variations in the heterogeneity of sampled conformations for the different IDP sequences provide a structural explanation for the calculated distributions of R_{ee} and R_g, which are clearly masked if only their mean values are analyzed. It is indeed remarkable that although the mean values of R_g and R_h adhere to Flory scaling laws for good solvents, there is considerable fine structure in the IDP ensembles, as the clustering analyses demonstrate. It is likely that the plasticity of the conformational ensembles makes it possible for IDPs to carry out diverse functional roles in a bewildering array of metabolic pathways.

DISCUSSION

Enhancements in Local Contact Probability Lead to Deviation from RC Behavior.

Ahallmark of polymers in good solvents (RCs) is that the $P(R_{ee})$ must obey the theoretical distribution obtained using polymer theory (see the Supporting Information). The statistical properties of the ensemble of conformations of RCs are purely determined only by chain entropy. Interestingly, we find that although the dependence of R_g on N_T for all the IDPs is consistent with the Flory scaling law (Figure 3), there are deviations in $P(R_{ee})$ from the expected theoretical predictions for RCs. For example, we observed such deviations for α-Synuclein, Prothymosin-α, as well as the Tau sequences K25, K23, K44, hTau23, and hTau40, but not for An16. The apparent conundrum can be understood from the dendrograms, which reveal clearly the sequence-dependent conformational heterogeneity. As a result, the conformational ensembles are determined not only by entropy, but also sequence-dependent energy, resulting in higher Boltzmann weights for certain classes of conformations relative to others.

To further illustrate the origin of deviation from the RC behavior, we calculated ensemble-averaged contact maps from simulations using the SOP-IDP energy function, as well as the corresponding RC limit. We define the difference contact maps as

$$\Delta C(i,j) = C_{\mathrm{IDP}}(i,j) - C_{\mathrm{RC}}(i,j) \quad (7)$$

where $C_{\mathrm{IDP}}(i,j)$ is the contact probability between residues i,j of an IDP obtained from simulations and $C_{\mathrm{RC}}(i,j)$ is the same contact probability obtained by specifically neglecting the contributions because of the last four terms in eq 1 (see the Methods section). Thus, $\Delta C(i,j)$ is a measure of the increased or decreased probability of contact between two residues, compared to an equivalent RC. Both $C_{\mathrm{IDP}}(i,j)$ and $C_{\mathrm{RC}}(i,j)$ were computed using the coordinates of the SC beads, including glycine and alanine. We assume that a contact exists if the distance between two residues is ≤0.8 nm.

The three contact maps shown in Figure 8 represent characteristically divergent scenarios.

An16.—The contact map for An16 (Figure 8a) shows a uniform enhancement in contacts between residues proximate along the sequence over the entire sequence length compared to an equivalent RC polymer. This can readily be understood as a consequence of the nonspecific attractive interactions between nonbonded residues, with sequence-specific interactions (final term in eq 1) playing a relatively minor role. Without the formation of stable local structures, such enhanced contacts do not alter the RC-like nature of the polymer, as also evidenced by the RC-like $P(R_{\mathrm{ee}})$ distribution for An16 (Figure 4).

K25.—The results in Figure 8b show that the K25 Tau construct contains a locally compact segment, with preferentially enhanced contacts compared to the rest of the sequence. The segment with locally enhanced contacts is also present in the WT Tau sequence (hTau40), as well as the K25, K23, K44, and hTau23 constructs (shown in Figures S15 and S16). We infer that the presence of this region, which results in the formation of the locally preferred structures, leads to the observed deviations from the RC-like behavior for the five sequence constructs.

Prothymosin-α.—In this IDP (Figure 8c), the two termini adopt locally compact structures, while the mid-segment of the IDP closely conforms to the RC limit. For this IDP, electrostatic interactions dominate the conformational properties, and the termini, with both positively and negatively charged residues, undergo local compaction. However, both the termini are overall negative, leading to unfavorable local electrostatic interactions. Both these effects together lead to the predominance of extended as well as relatively compact conformations in the conformational ensemble (Figure 7).

Structural Ensemble of a-Synuclein.

Our simulations provide considerable insights into the structural details of α-Synuclein, which has been extensively investigated using a variety of experimental methods. The calculated hydrodynamic radius reported in Table S3 (R_{h} = 2.89 ± 0.17 nm) is in very good agreement with the experimental value (R_{h} = 2.74 ± 0.04 nm) obtained using pulse field gradient NMR.[86] Similarly, the calculated R_{g} value is in close agreement with the experimental estimate (see Table S3), with the difference between simulation and experimental estimates being about 12%. More importantly, our simulations provide a complete characterization of the subtle structural details that are difficult to glean from

experiments. First, the segregation of the conformational landscape for α-Synuclein is in accord with recent experimental works [87–90] that hinted at the presence of distinct conformational states in the structural ensemble, with compact structures having the highest population at equilibrium. Specifically, the difference contact map (Figure 9) reveals that there are long-range tertiary interactions between residues in the acidic C-terminal region and the nascent polypeptide-associated complex (NAC) domain in α-Synuclein. Previous works[91,92] suggest that such interactions, which protect the NAC region against fibrillation, play a key role in impeding aggregation. Interestingly, tertiary contacts between residues in the neighborhood of 74 and 94, first noted in experiments using electron transfer,[93,94] are captured in the contact maps presented in Figure 9. Because of large conformational fluctuations of such tertiary interactions, which could serve as initiating nucleation sites for aggregation, the probability of forming such contacts is not substantial but detectable.

Sequence-specific deviations from the RC limit highlight the heterogeneity in the population of IDPs. We reiterate that it cannot be trivially ascertained that water (or solution conditions used in experiments) acts uniformly as a good solvent over the entire peptide sequence of an IDP. To classify IDP sequences as polymers in a good solvent, based solely on estimates of the Flory exponent ν with modest variations in N_T, is erroneous, which severely undermines the heterogeneity of their conformations.

Limitations of the SOP-IDP Model.

Although the SOP-IDP model is remarkably successful in capturing many aspects of the structural ensembles of even large IDPs, like all other empirical potentials, it is not without limitations. The SOP-IDP force field does reproduce quantitatively the radius of gyration of globular proteins at high denaturant concentrations, thus showing that the model is accurate in describing statistical properties of disordered states. It is unlikely that the model could predict the folding properties of even small globular proteins (e.g., the heat capacity) as a function of denaturant concentration as accurately as we have done here for $I(q)$ for IDPs.

Recently, the goal[35,37,38] of creating a transferable force field, which yields highly accurate results for both globular proteins and IDPs from essentially sequence alone, has been a motivating factor to drastically alter the currently popular force fields. Although laudable, achieving this goal is a daunting task because it is tantamount to solving all aspects of the protein folding problem and issues in IDPs in one fell swoop. In these studies,[35,37,38] which use three entirely different empirical energy functions, the calculated $I(q)$s for the 24-residue RS peptide (see the Supporting Information for details) and the 71-residue ACTR IDPs are in very good agreement with experiments. In addition, the R_g values for a few IDPs calculated using a force field[37] that differs greatly from the ones used by others[35,38] agree with experimental measurements. However, for foldable peptides and miniproteins, the agreement between simulations and experiments is not satisfactory, which means the stated goal of creating a transferable force field has not been accomplished. This illustrates the difficulty in building a truly “universal” potential within the limitations inherent in additive classical force fields, as articulated elsewhere.[38] With the possible exception of a recent study of IDPs,[37] applications (especially to globular proteins) are restricted to small N_T values, thus leaving open the question of the extent of transferability for longer N_T, even

when restricted to IDPs. It is indeed the case that a large number of energy functions, at all levels of coarse graining, could be constructed for successful applications to possibly only a certain class of proteins.

The SOP-IDP force field is not designed to be a universal potential that can simultaneously describe accurately the measurable properties of both IDPs and globular proteins. We have shown that the SOP-IDP force field is unique in its accuracy for IDPs, and provides a new perspective for describing their sequence-specific properties (and by statistical equivalence the DSE of globular proteins at high denaturant concentrations). However, for structural characterization of folded proteins under physiological conditions, as well as studies of various aspects of protein folding, the parameters described in Liu et al.[48] are appropriate. The one advantage is that the SOP model has only three independent parameters, and hence, a broad range of applications could be explored to assess its limitations.

Additional Tests.

We have taken advantage of the availability of experimental data and results from atomic detailed simulations of Wu et al.[38] to carry out simulations for the 24-residue RS peptide using the SOP-IDP model. Wu et al.[38] used the RSFF2+/TIP4P-D force field to calculate the scattering profile ($I(q)$ vs q) for the RS peptide and found it to be in excellent agreement with SAXS experiments. We used the current model to simulate the RS peptide and find that the $I(q)$s from the SOP-IDP model, the all-atom simulations, and the measured SAXS profile nicely overlap with each other (see Figure S4 in the Supporting Information). In the Supporting Information, we also illustrate additional applications to the 20-residue GS10 and the 26-residue HIV-1 Rev peptides for which R_g values (but not SAXS profiles) have been reported by Wu et al.[38] The results using coarse-grained and RSFF2+/TIP4P-D force fields are in good agreement. It should be pointed out that a similar level of accuracy could be obtained using the Flory formula given in the caption of Figure 3a, without the need for *any* simulations, which shows that the success of a force field can only be assessed by comparing the simulated and measured SAXS profiles. The predictions in the Supporting Information as well as the results in the main text show vividly that the proposed SOP-IDP energy function is highly efficacious in obtaining statistical properties of 27 IDPs of which 5 were used in the training set.

CONCLUSIONS

Given the multifarious roles that IDPs play in a variety of cellular functions, there is an urgent need to decipher the physical principles governing IDP structure, and dynamics, at the molecular level. We have introduced a robust coarse-grained model for IDPs (SOP-IDP), which quantitatively reproduces the SAXS profiles for a diverse range of sequences and length varying from 24 to 441 residues. The parameters of the force field were calibrated via a learning procedure, using a few test sequences, and once optimized they were unaltered for 24 other IDP sequences of varying composition, charge densities, and sequence lengths.

Although globally the sizes of the IDPs follow the well-known Flory scaling law obtained for synthetic polymers, equilibrium populations of different substates strongly depend on the precise IDP sequence. In the conformational substates of IDPs, we find evidence for specific

weak intramolecular interactions between certain residues, giving rise to population of conformations with local structures. We also show that the adaptability of IDPs arising from their conformational plasticity, which cannot be anticipated using sequence characteristics (such as fraction of positively and negatively charged residues) alone,[27] is important in their ability to interact with a multitude of partners to form fuzzy complexes stabilized by specific intermolecular interactions. Our work lends further credence to an existing viewpoint that the observed sequence-dependent conformational heterogeneity determines the functions of IDPs. The accuracy of the computations in describing the equilibrium ensemble of a number of IDPs sets the stage for describing IDP- RNA interactions, which is needed to understand ribonucleo-protein stress granule formation in eukaryotes, as well as quantitative descriptions of the formation of biomolecular condensates at the molecular level.

Supplementary Material

Refer to Web version on PubMed Central for supplementary material.

ACKNOWLEDGMENTS

We are indebted to Prof. D. I. Svergun for providing us with the tabulated forms of the scattering profiles for the Tau sequences, which enabled us to calibrate the SOP-IDP model. We thank Robert Best for providing the latest unpublished simulated scattering profiles ($I(q)$ vs q) for ACTR, Liz Rhoades for pointing out pertinent references, and Monika Fuxreiter for useful discussions. The research was supported by the National Science Foundation (CHE 16–36424), the Collie Welch Regents Chair (F-0019), and the National Institutes of Health (R01 GM107703 and GM089685). We are grateful to the Texas Advanced Computing Center (TACC) for providing the needed computing time.

REFERENCES

(1). Babu MM; van der Lee R; de Groot NS; Gsponer J. Intrinsically disordered proteins: regulation and disease. Curr. Opin. Struct. Biol. 2011, 21, 432–440. [PubMed: 21514144]

(2). Wright PE; Dyson HJ Intrinsically disordered proteins in cellular signalling and regulation. Nat. Rev. Mol. CellBiol. 2015,16, 18–29.

(3). Uversky VN; Oldfield CJ; Dunker AK Intrinsically disordered proteins in human diseases: introducing the D2 concept. Annu. Rev. Biophys. 2008, 37, 215–246. [PubMed: 18573080]

(4). Babu MM The contribution of intrinsically disordered regions to protein function, cellular complexity, and human disease. Biochem. Soc. Trans. 2016, 44, 1185–1200. [PubMed: 27911701]

(5). Iakoucheva LM; Brown CJ; Lawson JD; Obradović Z; Dunker AK Intrinsic disorder in cell-signaling and cancer-associated proteins. J. Mol. Biol. 2002, 323, 573–584. [PubMed: 12381310]

(6). Gsponer J; Babu MM Cellular strategies for regulating functional and nonfunctional protein aggregation. Cell Rep. 2012, 2, 1425–1437. [PubMed: 23168257]

(7). Tompa P. Intrinsically disordered proteins: a 10-year recap. Trends Biochem. Sci. 2012, 37, 509–516. [PubMed: 22989858]

(8). Hyman AA; Weber CA; Jülicher F. Liquid-liquid phase separation in biology. Annu. Rev. Cell Dev. Biol. 2014, 30, 39–58. [PubMed: 25288112]

(9). Busch DJ; Houser JR; Hayden CC; Sherman MB; Lafer EM; Stachowiak JC Intrinsically disordered proteins drive membrane curvature. Nat. Commun. 2015, 6, 7875. [PubMed: 26204806]

(10). Dima RI; Thirumalai D. Proteins associated with diseases show enhanced sequence correlation between charged residues. Bioinformatics 2004, 20, 2345–2354. [PubMed: 15073020]

(11). Shin Y; Brangwynne CP Liquid phase condensation in cell physiology and disease. Science 2017, 357, No. eaaf4382.

(12). Wright PE; Dyson HJ Linking folding and binding. Curr. Opin. Struct. Biol. 2009, 19, 31–38. [PubMed: 19157855]

(13). de Sancho D; Baker CM; Best RB In Computational Approaches to Protein Dynamics: From Quantum to Coarse-Grained Methods; Fuxreiter M, Ed.; CRC Press/Taylor&Francis: Boca Raton, U.S.A., 2015; pp 283–304.

(14). Brangwynne CP; Tompa P; Pappu RV Polymer physics of intracellular phase transitions. Nat. Phys. 2015, 11, 899–904.

(15). Dignon GL; Zheng W; Kim YC; Best RB; Mittal J. Sequence determinants of protein phase behavior from a coarse-grained model. PLoS Comput. Biol. 2018, 14, No. e1005941.

(16). Liu Y; Wang X; Liu B. A comprehensive review and comparison of existing computational methods for intrinsically disordered protein and region prediction. Briefings Bioinf. 2017, 20, 330–346.

(17). Levine ZA; Shea J-E Simulations of disordered proteins and systems with conformational heterogeneity. Curr. Opin. Struct. Biol. 2017, 43, 95–103. [PubMed: 27988422]

(18). Potenza E; Di Domenico T; Walsh I; Tosatto SCE MobiDB 2.0: an improved database of intrinsically disordered and mobile proteins. Nucleic Acids Res. 2015, 43, D315–D320. [PubMed: 25361972]

(19). Das RK; Ruff KM; Pappu RV Relating sequence encoded information to form and function of intrinsically disordered proteins. Curr. Opin. Struct. Biol. 2015, 32, 102–112. [PubMed: 25863585]

(20). Wright PE; Dyson HJ Intrinsically unstructured proteins: re-assessing the protein structure-function paradigm. J. Mol. Biol. 1999, 293, 321–331. [PubMed: 10550212]

(21). Schuler B; Soranno A; Hofmann H; Nettels D. Single-molecule FRET spectroscopy and the polymer physics ofunfolded and intrinsically disordered proteins. Annu. Rev. Biophys. 2016, 45, 207–231. [PubMed: 27145874]

(22). Kohn JE; Millett IS; Jacob J; Zagrovic B; Dillon TM; Cingel N; Dothager RS; Seifert S; Thiyagarajan P; Sosnick TR; et al. Random-coil behavior and the dimensions of chemically unfolded proteins. Proc. Natl. Acad. Sci. U.SA. 2004, 101, 12491–12496.

(23). Wilson DK; Grimshaw SB; Receveur V; Dobson CM; Jones JA; Smith LJ Hydrodynamic radii of native and denatured proteins measured by pulse field gradient NMR techniques. Biochemistry 1999, 38, 16424–16431. [PubMed: 10600103]

(24). Receveur-Brechot V; Durand D. How random are intrinsically disordered proteins? A small angle scattering perspective. Curr. Protein Pept. Sci. 2012, 13, 55–75. [PubMed: 22044150]

(25). Tamiola K; Acar B; Mulder FAA Sequence-specific random coil chemical shifts of intrinsically disordered proteins. J. Am. Chem. Soc. 2010, 132, 18000–18003. [PubMed: 21128621]

(26). Samanta HS; Zhuravlev PI; Hinczewski M; Hori N; Chakrabarti S; Thirumalai D. Protein collapse is encoded in the folded state architecture. Soft Matter 2017, 13, 3622–3638. [PubMed: 28447708]

(27). Samanta HS; Chakraborty D; Thirumalai D. Charge fluctuation effects on the shape of flexible polyampholytes with applications to intrinsically disordered proteins. J. Chem. Phys. 2018, 149, 163323.

(28). Bernadó P; Svergun DI Structural analysis of intrinsically disordered proteins by small-angle X-ray scattering. Mol. BioSyst. 2012, 8, 151–167. [PubMed: 21947276]

(29). Gibbs EB; Cook EC; Showalter SA Application of NMR to studies of intrinsically disordered proteins. Arch. Biochem. Biophys. 2017, 628, 57–70. [PubMed: 28502465]

(30). Brucale M; Schuler B; Samorí B. Single-molecule studies of intrinsically disordered proteins. Chem. Rev. 2014, 114, 3281–3317. [PubMed: 24432838]

(31). Fu B; Vendruscolo M. In Intrinsically Disordered Proteins Studied by NMR Spectroscopy; Felli IC, Pierattelli R, Eds.; Springer International Publishing: Cham, Switzerland, 2015; pp 35–48.

(32). Doi M; Edwards SF The Theory of Polymer Dynamics; Oxford University Press: New York, U. S. A., 1988.

(33). Kikhney AG; Svergun DI A practical guide to small angle X- ray scattering (SAXS) of flexible and intrinsically disordered proteins. FEBS Lett. 2015, 589, 2570–2577. [PubMed: 26320411]

(34). Piana S; Klepeis JL; Shaw DE Assessing the accuracy of physical models used in protein-folding simulations: quantitative evidence from long molecular dynamics simulations. Curr. Opin. Struct. Biol. 2014, 24,98–105. [PubMed: 24463371]

(35). Best RB; Zheng W; Mittal J. Balanced protein-water interactions improve properties of disordered proteins and non-specific protein association. J. Chem. Theory Comput. 2014, 10, 5113–5124. [PubMed: 25400522]

(36). Piana S; Donchev AG; Robustelli P; Shaw DE Water dispersion interactions strongly influence simulated structural properties of disordered protein states. J. Phys. Chem. B 2015, 119, 5113–5123. [PubMed: 25764013]

(37). Robustelli P; Piana S; Shaw DE Developing a molecular dynamics force field for both folded and disordered protein states. Proc. Natl. Acad. Sci. U.SA 2018, 115, 4758–4766.

(38). Wu H-N; Jiang F; Wu Y-D Significantly improved protein folding thermodynamics using a dispersion-corrected water model and a new residue-specific force field. J. Phys. Chem. Lett 2017, 8, 3199–3205. [PubMed: 28651056]

(39). Rauscher S; Gapsys V; Gajda MJ; Zweckstetter M; de Groot BL; Grübmuller H. Structural ensembles of intrinsically disordered proteins depend strongly on force field: a comparison to experiment. J. Chem. Theory Comput. 2015, 11, 5513–5524. [PubMed: 26574339]

(40). Henriques J; Cragnell C; Skepo M. Molecular dynamics simulations of intrinsically disordered proteins: force field evaluation and comparison with experiment. J. Chem. Theory Comput. 2015, 11, 3420–3431. [PubMed: 26575776]

(41). Cragnell C; Rieloff E; Skepö M. Utilizing coarse-grained modeling and monte carlo simulations to evaluate the conformational ensemble of intrinsically disordered proteins and regions. J. Mol. Biol. 2018, 430, 2478–2492. [PubMed: 29573987]

(42). Wu H; Wolynes PG; Papoian GA AWSEM-IDP: A Coarse-Grained Force Field for Intrinsically Disordered Proteins. J. Phys. Chem. B 2018, 122, 11115–11125. [PubMed: 30091924]

(43). Reddy G; Thirumalai D. Dissecting ubiquitin folding using the self-organized polymer model. J. Phys. Chem. B 2015, 119, 11358–11370. [PubMed: 26131594]

(44). Liu Z; Reddy G; Thirumalai D. Theory of the molecular transfer model for proteins with applications to the folding of the src-SH3 Domain. J. Phys. Chem. B 2012, 116, 6707–6716. [PubMed: 22497652]

(45). Fisher KM; Haglund E; Noel JK; Hailey KL; Onuchic JN; Jennings PA Geometrical frustration in Interleukin-33 decouples the dynamics of the functional element from the folding transition state ensemble. PLoS One 2015, 10, No. e0144067.

(46). Tehver R; Thirumalai D. Rigor to post-rigor transition in myosin V: link between the dynamics and the supporting architecture. Structure 2010, 18, 471–481. [PubMed: 20399184]

(47). Betancourt MR; Thirumalai D. Pair potentials for protein folding: choice of reference states and sensitivity of predicted native states to variations in the interaction schemes. Protein Sci. 1999, 8,361–369. [PubMed: 10048329]

(48). Liu Z; Reddy G; O'Brien EP; Thirumalai D. Collapse kinetics and chevron plots from simulations of denaturant-dependent folding of globular proteins. Proc. Natl. Acad. Sci. U.SA. 2011, 108, 7787–7792.

(49). Gates ZP; Baxa MC; Yu W; Riback JA; Li H; Roux B; Kent SBH; Sosnick TR Perplexing cooperative folding and stability of a low-sequence complexity, polyproline 2 protein lacking a hydrophobic core. Proc. Natl. Acad. Sci. U.SA. 2017, 114, 2241–2246.

(50). Reddy G; Thirumalai D. Collapse precedes folding in denaturant-dependent assembly of ubiquitin. J. Phys. Chem. B 2017, 121,995–1009. [PubMed: 28076957]

(51). Plimpto S. Fast Parallel Algorithms for Short-Range Molecular Dynamics. J. Comp. Physiol. 1995, 117, 1–19.

(52). Schneider T; Stoll E. Molecular-dynamics study of a three-dimensional one-component model for distortive phase transitions. Phys. Rev. B: Solid State 1978, 17, 1302–1322.

(53). Humphrey W; Dalke A; Schulten K. VMD: Visual molecular dynamics. J. Mol. Graphics Modell 1996, 14, 33–38.

(54). Tong D; Yang S; Lu L. Accurate optimization of amino acid form factors for computing small-angle X-ray scattering intensity of atomistic protein structures. J. Appl Crystallogr. 2016, 49, 1148–1161. [PubMed: 28074088]

(55). Stetefeld J; McKenna SA; Patel TR Dynamic light scattering: a practical guide and applications in biomedical sciences. Biophys. Rev. 2016, 8, 409–427. [PubMed: 28510011]

(56). Sherman E; Itkin A; Kuttner YY; Rhoades E; Amir D; Haas E; Haran G. Using fluorescence correlation spectroscopy to study conformational changes in denatured proteins. Biophys. J. 2008, 94,4819–4827. [PubMed: 18326651]

(57). Gast K; Fiedler C. Intrinsically disordered protein analysis In Methods in Molecular Biology (Methods and Protocols); Uversky V, Dunker, Eds.; Springer: New York, NY, U.S.A., 2012; pp 137–161.

(58). Hyeon C; Dima RI; Thirumalai D. Size, shape, and flexibility of RNA structures. J. Chem. Phys. 2006, 125, 194905.

(59). Dima RI; Thirumalai D. Asymmetry in the Shapes of Folded and Denatured States of Proteins. J. Phys. Chem. B 2004, 108, 6564–6570.

(60). Aronovitz JA; Nelson DR Universal features of polymer shapes. J. Phys. 1986, 47, 1445–1456.

(61). Data Mining and Knowledge Discovery Handbook, 2nd ed.; Maimon O, Rokach L, Eds.; Springer: New York, U. S. A., 2010.

(62). Ward JH Hierarchical grouping to optimize an objective function. J. Am. Stat. Assoc. 1963, 58, 236–244.

(63). Cragnell C; Durand D; Cabane B; Skepo M. Coarse-grained modeling of the intrinsically disordered protein Histatin 5 in solution: Monte Carlo simulations in combination with SAXS. Proteins: Struct., Fund, Bioinf 2016, 84, 777–791.

(64). Kjaergaard M; Norholm A-B; Hendus-Altenburger R; Pedersen SF; Poulsen FM; Kragelund BB Temperature- dependent structural changes in intrinsically disordered proteins: Formation of a-helices or loss of polyproline II? Protein Sci. 2010, 19, 1555–1564. [PubMed: 20556825]

(65). Mercadante D; Milles S; Fuertes G; Svergun DI; Lemke EA; Gräter F. Kirkwood-Buff Approach Rescues Overcollapse of a Disordered Protein in Canonical Protein Force Fields. J. Phys. Chem. B 2015, 119, 7975–7984. [PubMed: 26030189]

(66). Arbesú M; Maffei M; Cordeiro TN; Teixeira JMC; Pérez Y; Bernadó P; Roche S; Pons M. The unique domain forms a fuzzy intramolecular complex in Src family kinases. Structure 2017, 25, 630–640. [PubMed: 28319009]

(67). Mittag T; Marsh J; Grishaev A; Orlicky S; Lin H; Sicheri F; Tyers M; Forman-Kay JD Structure/function implications in a dynamic complex of the intrinsically disordered Sic1 with the Cdc4 subunit of an SCF ubiquitin ligase. Structure 2010, 18, 494–506. [PubMed: 20399186]

(68). Wells M; Tidow H; Rutherford TJ; Markwick P; Jensen MR; Mylonas E; Svergun DI; Blackledge M; Fersht AR Structure of tumor suppressor p53 and its intrinsically disordered N-terminal transactivation domain. Proc. Natl. Acad. Sci. U.S.A. 2008, 105, 5762–5767. [PubMed: 18391200]

(69). Uversky VN; Gillespie JR; Millett IS; Khodyakova AV; Vasilenko RN; Vasiliev AM; Rodionov IL; Kozlovskaya GD; Dolgikh DA; Fink AL; et al. Zn2+-mediated structure formation and compaction of the “natively unfolded” human Prothymosin a. Biochem. Biophys. Res. Commun. 2000, 267, 663–668. [PubMed: 10631119]

(70). Lens Z; Dewitte F; Monté D; Baert J-L; Bompard C; Sénérhal M; Van Lint C; de Launoit Y; Villeret V; Verger A. Solution structure of the N-terminal transactivation domain of ERM modified by SUMO-1. Biochem. Biophys. Res. Commun. 2010, 399, 104–110. [PubMed: 20647002]

(71). Schwalbe M; Ozenne V; Bibow S; Jaremko M; Jaremko L; Gajda M; Jensen MR; Biernat J; Becker S; Mandelkow E; et al. Predictive Atomic Resolution Descriptions of Intrinsically Disordered hTau40 and α-Synuclein in Solution from NMR and Small Angle Scattering. Structure 2014, 22, 238–249. [PubMed: 24361273]

(72). Nairn KM; Lyons RE; Mulder RJ; Mudie ST; Cookson DJ; Lesieur E; Kim M; Lau D; Scholes FH; Elvin CM A synthetic resilin is largely unstructured. Biophys. J. 2008, 95, 3358–3365. [PubMed: 18586853]

(73). Holt C; Sorensen ES; Clegg RA Role of calcium phosphate nanoclusters in the control of calcification. FEBS J. 2009, 276, 2308–2323. [PubMed: 19292864]

(74). Henriques J; Skepö M. Molecular dynamics simulations of intrinsically disordered proteins: on the accuracy of the TIP4P-D water model and the representativeness of protein disorder models. J. Chem. Theory Comput 2016, 12, 3407–3415. [PubMed: 27243806]

(75). Mylonas E; Hascher A; Bernadó P; Blackledge M; Mandelkow E; Svergun DI Domain Conformation of Tau Protein Studied by Solution Small-Angle X-ray Scattering. Biochemistry 2008, 47, 10345–10353. [PubMed: 18771286]

(76). Teraoka I. Polymer Solutions: An Introduction to Physical Properties; John Wiley & Sons: New York, U. S. A., 2002.

(77). Rubinstein M; Colby RH Polymer Physics; Oxford University Press: New York, U. S. A., 2003.

(78). Honeycutt JD; Thirumalai D. Static properties of polymer chains in porous media. J. Chem. Phys. 1989, 90, 4542–4559.

(79). Song J; Gomes G-N; Shi T; Gradinaru CC; Chan HS Conformational heterogeneity and FRET data interpretation for dimensions of unfolded proteins. Biophys. J. 2017, 113, 1012–1024. [PubMed: 28877485]

(80). Song J; Gomes G-N; Gradinaru CC; Chan HS; Chan HS An Adequate Account of Excluded Volume Is Necessary To Infer Compactness and Asphericity of Disordered Proteins by Förster Resonance Energy Transfer. J. Phys. Chem. B 2015,119, 15191–15202. [PubMed: 26566073]

(81). Fuertes G; Banterle N; Ruff KM; Chowdhury A; Mercadante D; Koehler C; Kachala M; Girona GE; Milles S; Mishra A; et al. Decoupling of size and shape fluctuations in heteropolymeric sequences reconciles discrepancies in SAXS vs FRET measurements. Proc. Natl. Acad. Sci. U.S.A. 2017, 114, E6342–E6351. [PubMed: 28716919]

(82). Riback JA; Bowman MA; Zmyslowski AM; Knoverek CR; Jumper JM; Hinshaw JR; Kaye EB; Freed KF; Clark PL; Sosnick TR Innovative scattering analysis shows that hydrophobic disordered proteins are expanded in water. Science 2017, 358,238–241. [PubMed: 29026044]

(83). Best RB; Zheng W; Borgia A; Buholzer K; Borgia MB; Hofmann H; Soranno A; Nettels D; Gast K; Grishaev A; et al. Comment on “Innovative scattering analysis shows that hydrophobic disordered proteins are expanded in water”. Science 2018, 361, 7101.

(84). Fuertes G; Banterle N; Ruff KM; Chowdhury A; Pappu RV; Svergun DI; Lemke EA Comment on “Innovative scattering analysis shows that hydrophobic disordered proteins are expanded in water”. Science 2018, 361, 8230.

(85). Zambelli AE A data-driven approach to estimating the number of clusters in hierarchical clustering. F1000Research 2016, 5, 2809.

(86). Sevcsik E; Trexler AJ; Dunn JM; Rhoades E. Allostery in a Disordered Protein: Oxidative Modifications to α-Synuclein Act Distally To Regulate Membrane Binding. J. Am. Chem. Soc. 2011, 133,7152–7158. [PubMed: 21491910]

(87). Frimpong AK; Abzalimov RR; Uversky VN; Kaltashov IA Characterization of intrinsically disordered proteins with electrospray ionization mass spectrometry: conformational heterogeneityof α-Synuclein. Proteins: Struct. Fund., Bioinf 2010, 78, 714–722.

(88). Nath A; Sammalkorpi M; DeWitt DC; Trexler AJ; Elbaum-Garfinkle S; O’Hern CS; Rhoades E. The Conformational Ensembles of α-Synuclein and Tau: Combining Single-Molecule FRET and Simulations. Biophys. J. 2012, 103, 1940–1949. [PubMed: 23199922]

(89). UIlman O; Fisher CK; Stultz CM Explaining the structural plasticity of α-Synuclein. J. Am. Chem. Soc. 2011, 133, 19536–19546. [PubMed: 22029383]

(90). Dedmon MM; Lindorff-Larsen K; Christodoulou J; Vendruscolo M; Dobson CM Mapping Long-Range Interactions in α-Synuclein using Spin-Label NMR and Ensemble Molecular Dynamics Simulations. J. Am. Chem. Soc. 2005, 127, 476–477. [PubMed: 15643843]

(91). Hoyer W; Cherny D; Subramaniam V; Jovin TM Impact of the Acidic C-Terminal Region Comprising Amino Acids 109–140 on a-Synuclein Aggregation in Vitro. Biochemistry 2004, 43, 16233–16242. [PubMed: 15610017]

(92). Trexler AJ; Rhoades E. Single Molecule Characterization of α-Synuclein in Aggregation-Prone States. Biophys. J. 2010, 99, 3048–3055. [PubMed: 21044603]

(93). Le JC.; Gra HB.; Winkle JR. Tertiary Contact Formation in α-Synuclein Probed by Electron Transfer. J. Am. Chem. Soc. 2005, 127, 16388–16389. [PubMed: 16305213]

(94). Lee JC; Lai BT; Kozak JJ; Gray HB; Winkler JR α-Synuclein Tertiary Contact Dynamics. J. Phys. Chem. B 2007, 111, 2107–2112. [PubMed: 17279794]

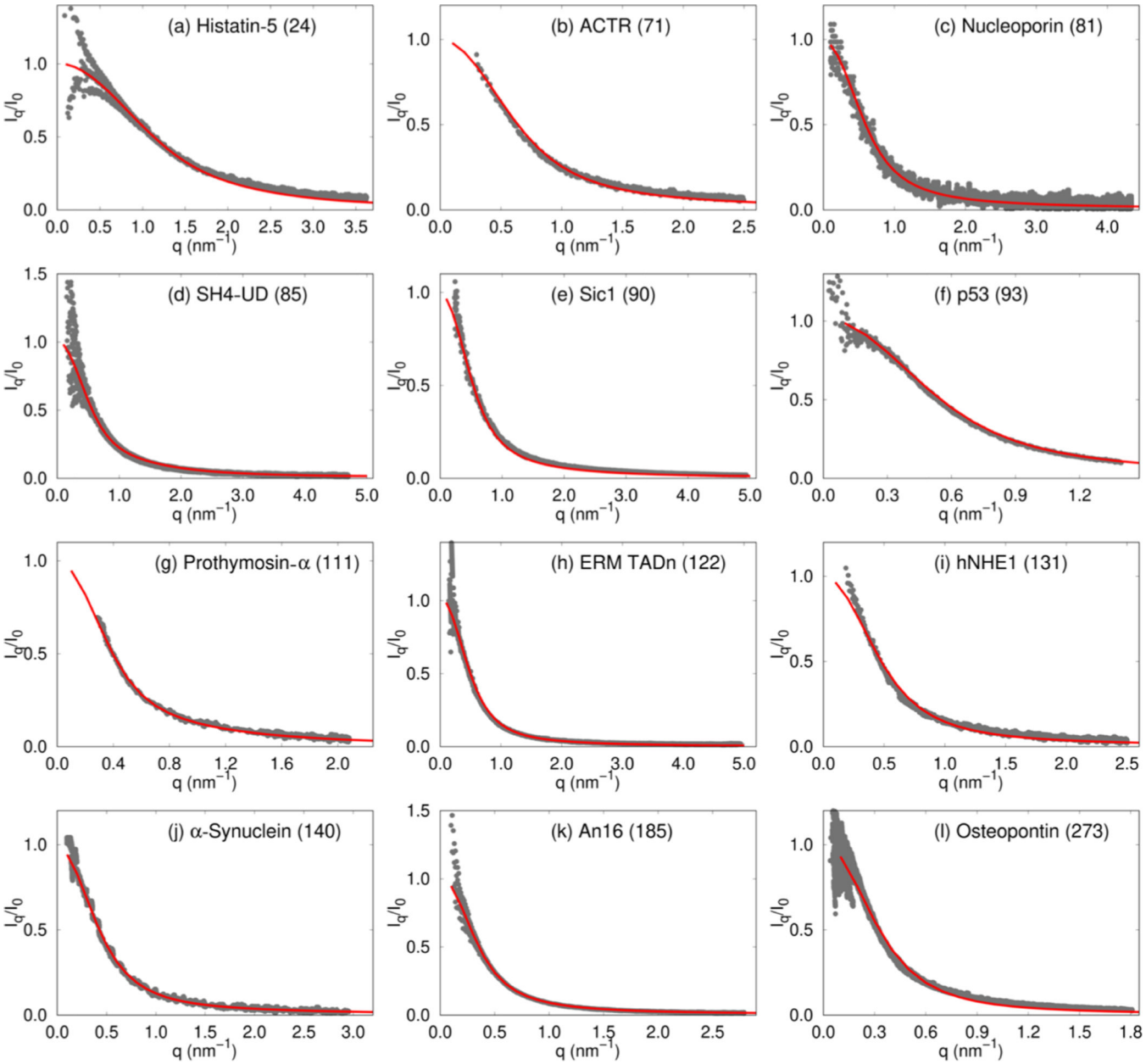

Figure 1.

Comparison of SAXS profiles for 12 IDPs, labeled in the panels. The experimental profiles[63–73] are shown using gray dots and those obtained from simulations are depicted using red curves. The number in parentheses in each figure is N_T, which indicates the number of residues in each IDP. Histatin-5 (a), ACTR (b), and hNHE1 (i) are part of the initial training set.

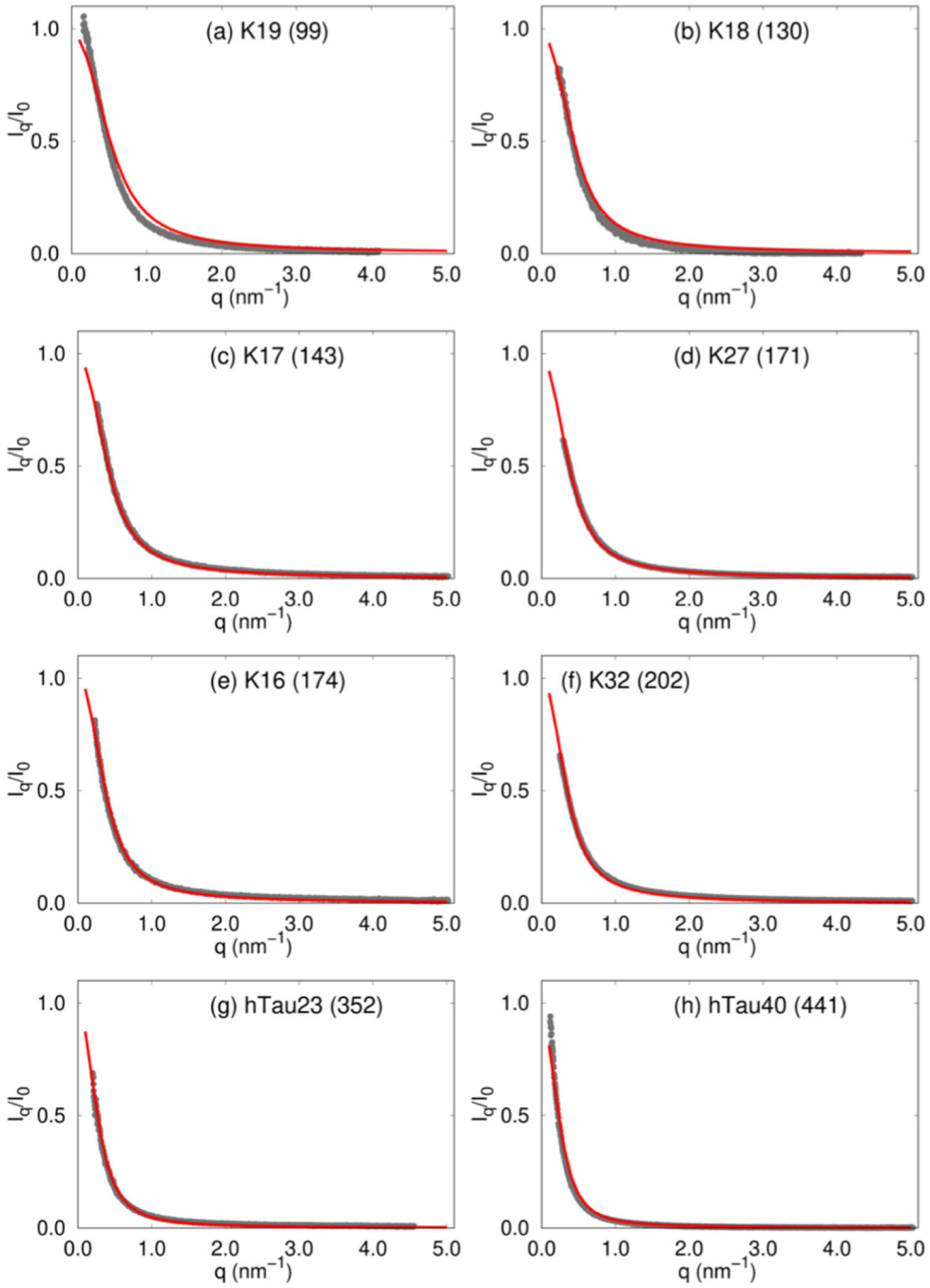

Figure 2.

Comparison of SAXS profiles for eight Tau protein constructs. The lengths of the sequences are shown in parentheses in each figure. The color coding is the same as in Figure 1.

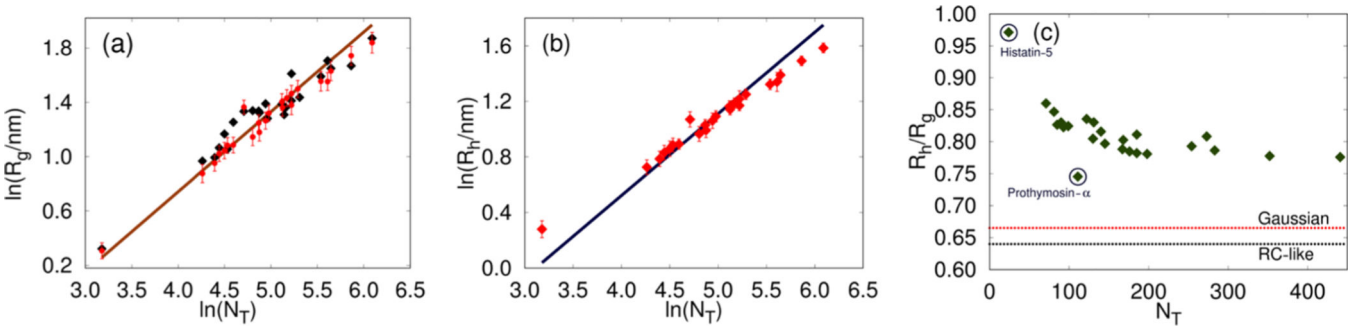

Figure 3.

(a) Values of R_g from simulations (red circles) in comparison with the experimental estimates (black squares).The brown solid line is a fit to the power law: $R_g = R_g^0 N^\nu$, with $R_g^0 = 0.2$ nm and $\nu = 0.588$.(b) Hydrodynamic radii, R_hs, of the IDPs computed from the simulation trajectories (red symbols). The solid blue line is a power law fit: $R_h = R_h^0 N^\nu$, with $\hat{R_h^0} = 0.16$ nm and $\nu = 0.588$. Both R_g and R_h follow the Flory random coil predictions. (c) Ratio of the hydrodynamic radius to the radius of gyration R_h/R_g obtained from simulations. The outliers, Histatin-5 and Prothymosin-α, are marked with circles. The theoretical limits are marked as dotted lines. Note that there are substantial deviations from the theoretical predictions for an ideal chain and a polymer in a good solvent.

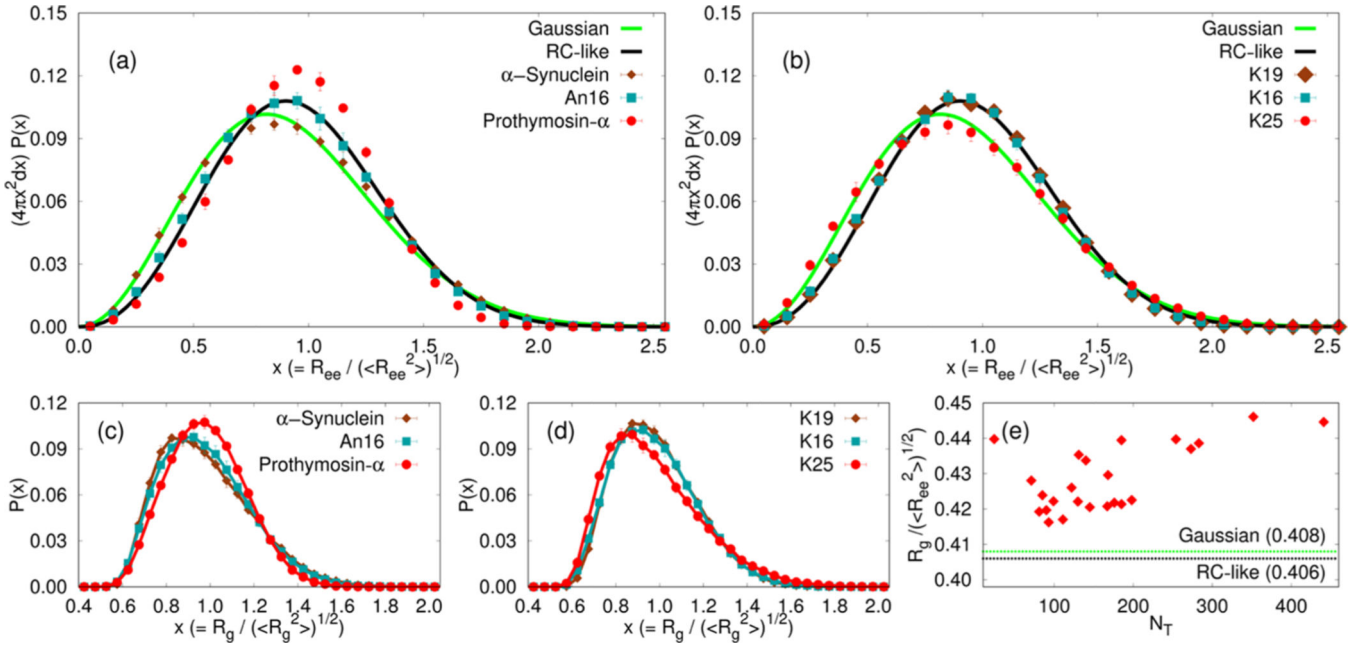

Figure 4.

Distributions of the end-end distance (R_{ee}), scaled by $\langle R_{ee}^2 \rangle^{1/2}$. In order to compare with results for Gaussian chains (solid green line) and RCs (solid black line), we show $4\pi x^2 P(x)$, where $x = R_{ee}/\langle R_{ee}^2 \rangle^{1/2}$. (a,b) show the distributions for representatives from the sets of non-Tau IDP sequences and Tau sequence constructs, respectively. If a particular IDP behaves strictly as a RC (Gaussian chain) in terms of end-end distance distribution, then the corresponding distribution should coincide exactly with the theoretical result in black (green). (c,d) Distributions of R_g for IDPs described in (a,b) respectively. (e) Ratio of R_g to root-mean-square R_{ee} for all 24 IDPs described in the article. The dashed horizontal lines in green and black show the ratio for a Gaussian chain and a RC, respectively.

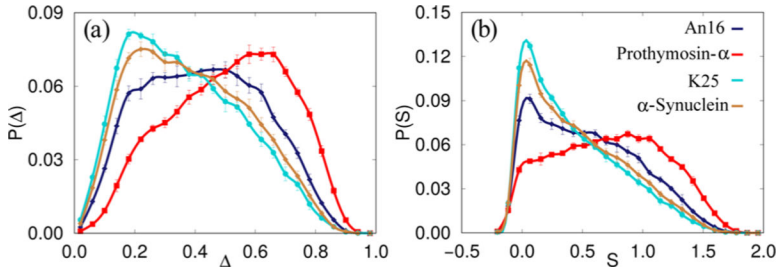

Figure 5.

Comparison of the distributions of shape parameters (a) Δ and (b) S for An16 (blue, diamonds), α-Synuclein (brown, diamonds), Prothymosin-α (red, squares), and K25 construct of the Tau protein (cyan, circles). Note that the average values of Δ and S for Gaussian chains are 0.52 and 0.87, respectively, and the corresponding estimates for an equivalent polymer in a good solvent are 0.55 and 0.91, respectively. The mean values of both Δ and S for the IDPs are drastically different from the expected theoretical values for standard polymer models.

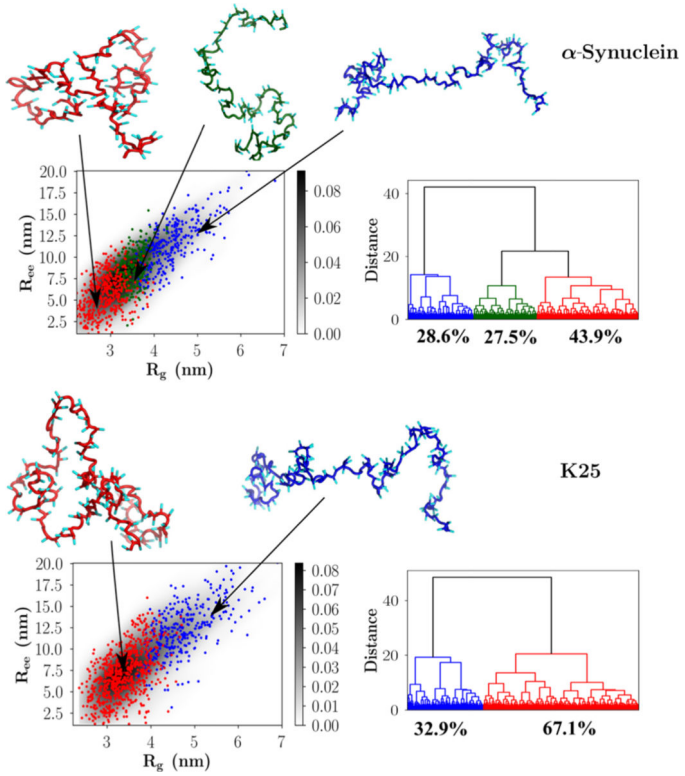

Figure 6.

Hierarchical clustering of the IDP conformational ensembles using the Ward variance minimization algorithm. Upper panel: α-Synuclein; lower panel: K25. The conformational landscapes (depicted as probability density plots) projected onto R_g and R_{ee} are shown on the left of each figure, and the corresponding dendrograms are shown on the right. Representative snapshots from each family, with their backbones rendered in different colors, are shown superposed on the conformational landscape. The same color-coding is used to classify clusters within the dendrograms and the two-dimensional plots. The relative cluster populations are marked below the appropriate dendrogram branches.

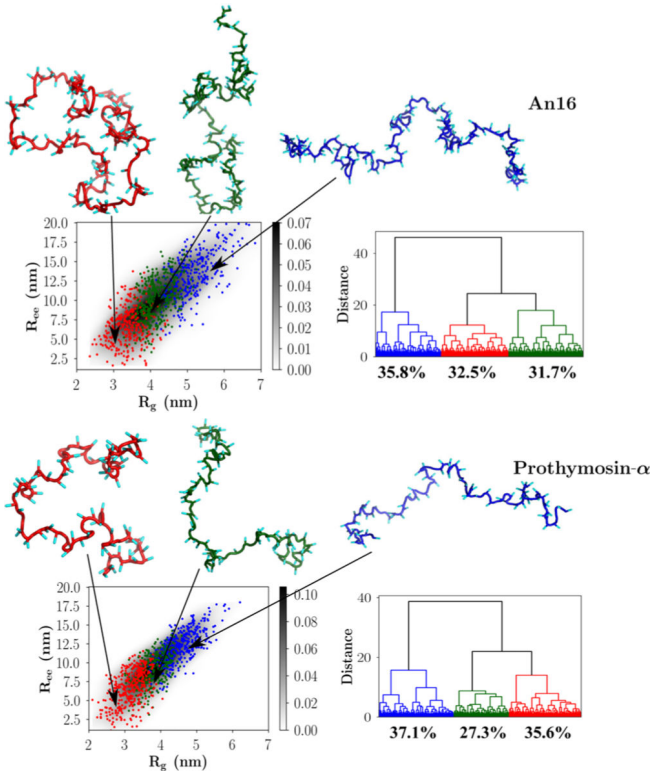

Figure 7.

Upper panel: An16; lower panel: Prothymosin-α. The conformational landscapes projected onto R_g and R_{ee} are shown on the left of each figure, and the corresponding dendrograms are shown on the right. Representative snapshots from each family, with their backbones rendered in different colors, are shown superposed on the conformational landscape. The same color-coding is used to classify clusters within the dendrograms and the two-dimensional plots. The relative cluster populations are marked below the appropriate dendrogram branches.

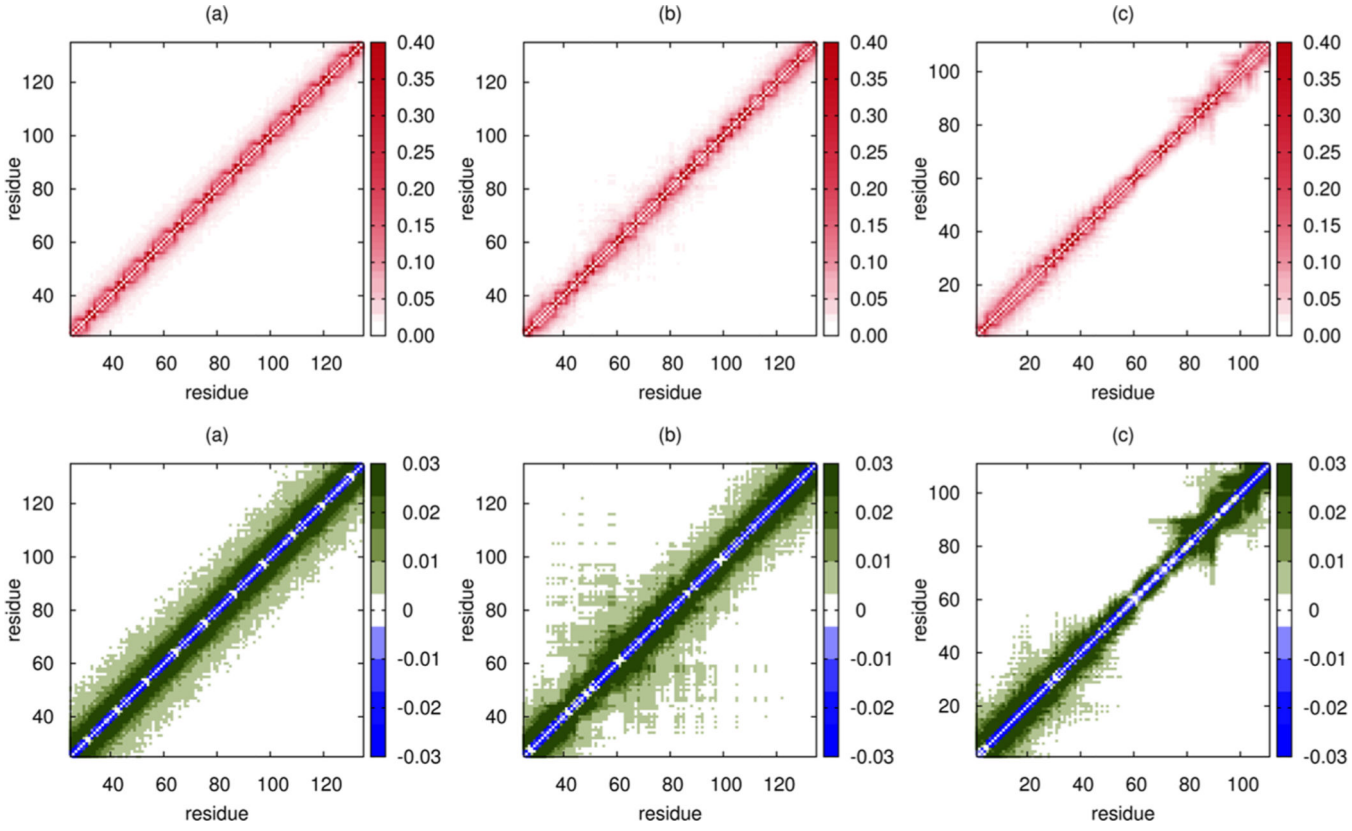

Figure 8.

Contact maps for (a) An16, (b) K25 Tau construct, and (c) Prothymosin-α. The top panel shows the contact maps for the three IDPs calculated using the SOP-IDP simulations. To illustrate the deviations from the corresponding RC contact map, we plot the difference map using eq 7 (bottom panel). While the contact map for An16 reveals no sequence-driven propensities for local structures, the latter two clearly highlight the presence of local domains that are more compact compared to the rest of the sequence. The nearly RC-like behavior of the mid-segment of Prothymosin-α, in stark contrast to the other IDPs studied (see also Figures S14–S16 in the Supporting Information), rationalizes the peripheral contribution of compact conformations observed for it in the hierarchical clustering of the conformational ensemble. Each of the contact maps depicts a segment of 111 residues (N_t for Prothymosin-α) for optimal visual comparison. The full ranges for (a) and (b) are shown in Figure S16 in the Supporting Information.

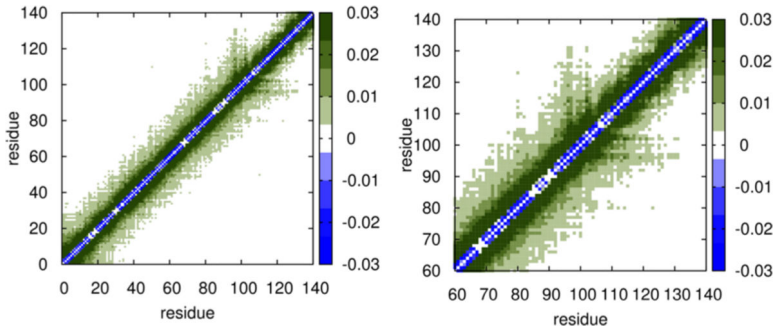

Figure 9.

Difference contact maps for α-Synuclein. Left: whole sequence; Right: zoomed-in view highlighting the contacts between the C-terminal and the NAC regions.